communications physics

A Nature Portfolio journal

Article

https://doi.org/10.1038/s42005-026-02668-7

Kibble-Zurek scaling and spatial statistics in quenched binary Bose superfluids

Check for updates

Subhadeep Patra [1], Arko Roy [1] ✉, Seong-Ho Shinn [2], Adolfo del Campo [2,3] & Mithun Thudiyangal [4]

The emergence of order from an initially uncorrelated state across a phase transition is a central problem in quantum many-body physics, particularly in multicomponent systems where interactions between components lead to rich nonequilibrium dynamics. While defect formation is known to follow universal scaling laws, prior studies have focused mainly on defect density, leaving their spatial organization largely unexplored. Here we show that gradually tuning the chemical potential in a two-dimensional binary Bose gas drives condensation into either a miscible or immiscible phase. In the immiscible regime, domains form whose number, size, and boundary length obey Kibble-Zurek (KZ) scaling and evolve self-similarly. In the miscible regime, vortices emerge with KZ scaling. In both cases, the spatial distribution of vortices and domains is well described by a Poisson point process with KZ-determined density. These results reveal universal features of far-from-equilibrium dynamics and provide a framework to characterize stochastic geometry in multicomponent quantum systems.

The dynamics of spontaneous symmetry breaking through phase transition has been studied in various fields, including cosmology[1–3], condensed matter physics[4–6], ultracold atom systems[7–10], and their use for quantum simulation[11–13]. Ultracold atomic gases provide an ideal testbed for studying such dynamics in a controlled and tunable manner. Furthermore, the ability to drive phase transitions in these systems enables direct probing of universal scaling laws, such as those predicted by the Kibble–Zurek mechanism (KZM)[1,7,10,14]. Ultracold gases thus provide a unique platform for exploring defect formation and critical dynamics in a nonequilibrium setting. The cooling dynamics of a thermal gas leading to the formation of a scalar Bose–Einstein condensate (BEC) of a single component is characterized by $U(1)$ symmetry breaking and can lead to the formation of solitons or vortices, depending on the dimensionality[15–23]. A richer arena is offered by spinor gases[9,24,25] and atomic mixtures[26]. For instance, in the case of Bose–Bose mixtures[27–29], two interacting superfluid components evolve under external tuning parameters, such as chemical potential or interaction strength. In these mixtures, phase transitions give rise to rich defect structures, including quantized vortices and spatial domains, whose formation reflects the interplay of microscopic interactions and collective critical dynamics.

The KZM theory predicts that the density of topological defects resulting from the critical dynamics scales as a universal power law of the quench time in which the transition is crossed, with the power-law exponent being determined by the critical exponents and the dimensionality of the system. To date, KZM has been studied in both classical and quantum phase transitions[10] and tested in various setups, including trapped bosonic gas[17,22,30–33], trapped ions[34–36], superconducting vortex systems[37,38], and Josephson junctions[39].

In this work, we investigate the formation of a Bose–Bose mixture driven by a linear quench of the chemical potential, resulting in the growth of either a miscible or an immiscible phase, depending on the inter- and intra-species interactions. This system provides the opportunity to study the formation of domains and vortices, as well as their universal dynamics, in a single platform. Domain formation has been explored in various ultracold systems, including spin-1 spin-orbit coupled BECs[40], binary BECs with internal coupling[41], and confined systems in elongated harmonic traps[42] and ring-shaped quasi-1D potentials[43]. Unlike coherently coupled spinor condensates where magnetization gradients develop across domain walls, here the two components are coupled only through density-density interactions, and spontaneous phase separation in the immiscible regime occurs purely via interaction energy minimization.

Using the stochastic (projected) Gross–Pitaevskii equation (SPGPE) in two dimensions[44,45] together with the quench protocol described in the "Methods", we focus on the symmetry-breaking dynamics following condensation from vacuum. First, in the immiscible phase, we show the number of domains, domain areas, domain wall lengths, at a characteristic equilibration time t_{eq} to obey universal power-law behavior with respect to the quench time τ_Q. The early-time collapse of domain wall length curves indicates the self-similar dynamics. Second, in the miscible phase, we demonstrate vortex formation and verify Kibble–Zurek (KZ) scaling of the

[1]School of Physical Sciences, Indian Institute of Technology Mandi, Mandi, India. [2]Department of Physics and Materials Science, University of Luxembourg, Luxembourg, Luxembourg. [3]Donostia International Physics Center, San Sebastián, Spain. [4]Center for Quantum Technologies and Complex Systems (CQTCS), Christ University, Bengaluru, India. ✉e-mail: arko@iitmandi.ac.in

vortex numbers. Finally, going beyond defect counting, we studied the universal spatial statistics of vortices in the miscible phase and mean domain positions in the immiscible phase, showing that their distributions are well described by Poisson point processes (PPP), uncovering universal non-equilibrium dynamics that lie beyond the scope of the KZM. These predictions are amenable to direct experimental verification using atomic mixtures in uniform traps, and can be applied to other fields, such as the circulation statistics or quantum turbulence.

Results and discussions

Condensate norm evolution and characterization of the equilibration time

With $\mathcal{A}$ being the area of the box, we monitor the growth of the norm $\mathcal{N}(t) = (1/\mathcal{A})\sum_{j=1,2}\iint|\psi_j(\mathbf{x}, t)|^2 d\mathbf{x}$ of the order parameter corresponding to the symmetry broken phases illustrated in Fig. 1 for different quench time τ_Q. Note that the final scaled number density of atoms represented by $\mathcal{N}$ shown in Fig. 1, is consistent with μ_f/g, where μ_f is the final chemical potential after the quench and g is the intra-species interaction strength (see the "Methods"). Details of the SPGPE formalism[44,45], along with a brief discussion of the numerical parameters, are provided in the Supplementary Methods. The onset of spontaneous symmetry breaking is signaled by a sharp increase in the condensate norm, illustrated in Fig. 1a, b, accompanied by the emergence of protodomains. In the early freeze-out stage ($t \ll t_{eq}$), the condensate is ill-defined and lacks coherent structure[46]. A physically meaningful timescale for analyzing the KZ scaling is the equilibration time t_{eq}, which marks the crossover from exponential to adiabatic linear growth shown in Fig. 1. The procedure for extracting t_{eq} is detailed in the Supplementary Note 1. At t_{eq}, which is proportional to the KZ freeze-out time, isolated protodomains begin to coalesce, signaling the onset of global order and symmetry breaking[46]. It follows the KZ scaling similar to that of the freeze-out time, such that $t_{eq} \propto \left(\tau_0 \tau_Q^{z\nu}\right)^{1/(1+z\nu)}$, with $z\nu = 1$, consistent with mean-field exponents $z = 2$, $\nu = 1/2$, and τ_0 being a system-dependent constant[16,23,47–49]. Based on our numerical analysis, we extract $t_{eq} = (4.97 \pm 0.072)\tau_Q^{0.48\pm0.002}$ for the growth to the immiscible phase characterized by $g_{12} > g$, with g_{12} being the inter-species interaction strength, and $t_{eq} = (5.13 \pm 0.064)\tau_Q^{0.48\pm0.002}$ for the growth to the miscible phase characterized by $g_{12} < g$. Note that in our system, the critical chemical potential μ_c, marking the symmetry breaking transition, is not crossed exactly at $t = 0$. While this could introduce corrections to the KZM freeze-out time, we find their effect negligible, with the scaling dominated by the standard KZ power law; see the Supplementary Note 1 for further details. The numerically obtained exponents match well with the KZM predictions. Deviations in the fast-quench regime ($\tau_Q < 20$) indicate a breakdown of KZ scaling, while the collapse of rescaled growth curves in Fig. 1c, d confirms the slow quench regime. These benchmarks aid to validate the KZM prediction for topological defect density[10,46,48,50]: $\rho \propto \left(\tau_0/\tau_Q\right)^{(D-d)\nu/(1+z\nu)}$, where D is the system dimension and d is the defect dimension (e.g., $d = 0$ for point defects). In general, thermal vortices may affect the KZ scaling on defect density. However, using the results in ref. 51, the number of thermal vortices per total number of bosons in the condensate is expected to be $\exp(-6.7 \times 10^6)$ for the parameters we used. Therefore, since the total number of bosons in the condensate is at most $\mathcal{N}(t)\mathcal{A} \approx 10^4$, the effect of the Berezinskii–Kosterlitz–Thouless (BKT) transition on the KZ scaling is negligible, as in the quasi-two-dimensional Bose gas experiment[52].

We further aim to capture the evolution of the condensate norm $\mathcal{N}(t)$ analytically. To this end, we consider the growth of the complex order parameter $\psi_j(\mathbf{x}, t)$ governed by the SPGPE in Eq. 7. By neglecting spatial dependence and stochastic noise, following Suzuki et al.[53], the stochastic partial differential equation can be reduced to an effective time-dependent ordinary differential equation, given by

$$(1 - i\gamma)(g|\psi_j(t)|^2\psi_j(t) + g_{12}|\psi_{3-j}(t)|^2\psi_j(t) - \mu(t)\psi_j(t)) = i\dot{\psi}_j(t), \quad (1)$$

where γ is the dissipation parameter and $\mu(t)$ is the chemical potential (see the "Methods" for details). Using Madelung transformation, Eq. 1 becomes

$$\dot{n}_T = 2\gamma\mu(t)n_T - \gamma(g + g_{12})(n_T^2 + n_M^2) - \gamma(g - g_{12})n_M^2. \quad (2)$$

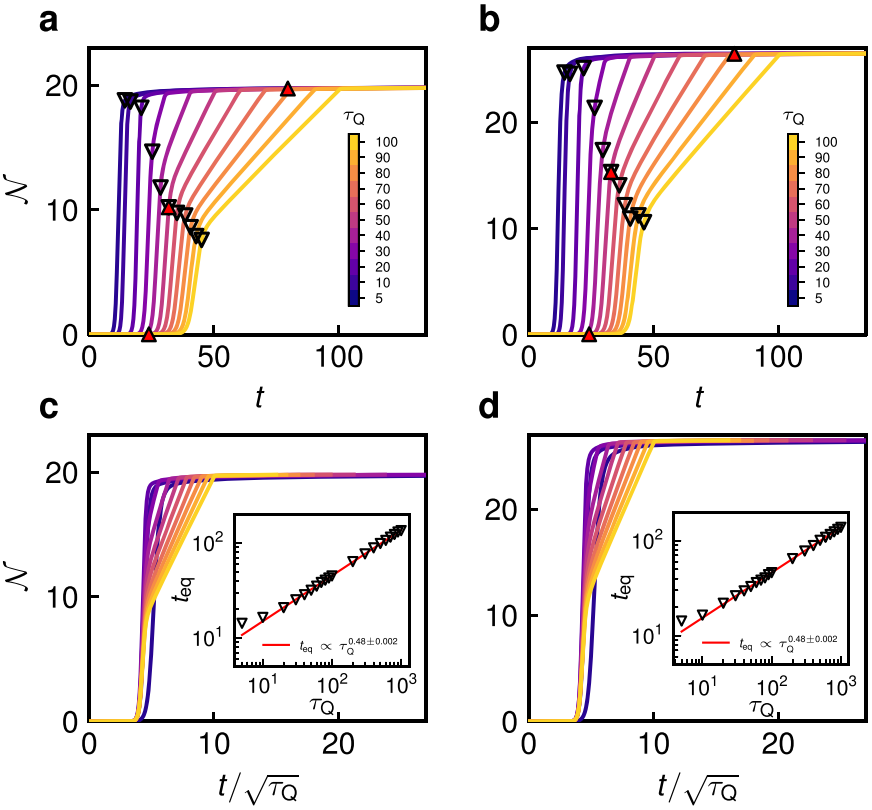


Fig. 1 | Scaled number density of atoms for various quench times. Norm $\mathcal{N}(t)$ that represents the scaled number density of atoms is plotted as a function of time t during growth into **a** immiscible and **b** miscible phases for quench times τ_Q = [5, 10, 20,…,100], arranged left to right for a single noise realization. The equilibration time t_{eq} (black triangles) scales as $t_{eq} \propto \tau_Q^{0.48\pm0.002}$ for $g_{12} > g$ [inset of (c)] and $t_{eq} \propto \tau_Q^{0.48\pm0.002}$ for $g_{12} < g$ [inset of (**d**)], shown by red lines, where g and g_{12} are the intra- and inter-species interaction strengths, respectively. **c**, **d** The early exponential growth ($t < t_{eq}$) collapses when time is scaled by $\tau_Q^{1/2}$, except for τ_Q = 5, 10. Filled red markers on τ_Q = 50 curves in (**a**, **b**) indicate times at which the density profiles are presented later.

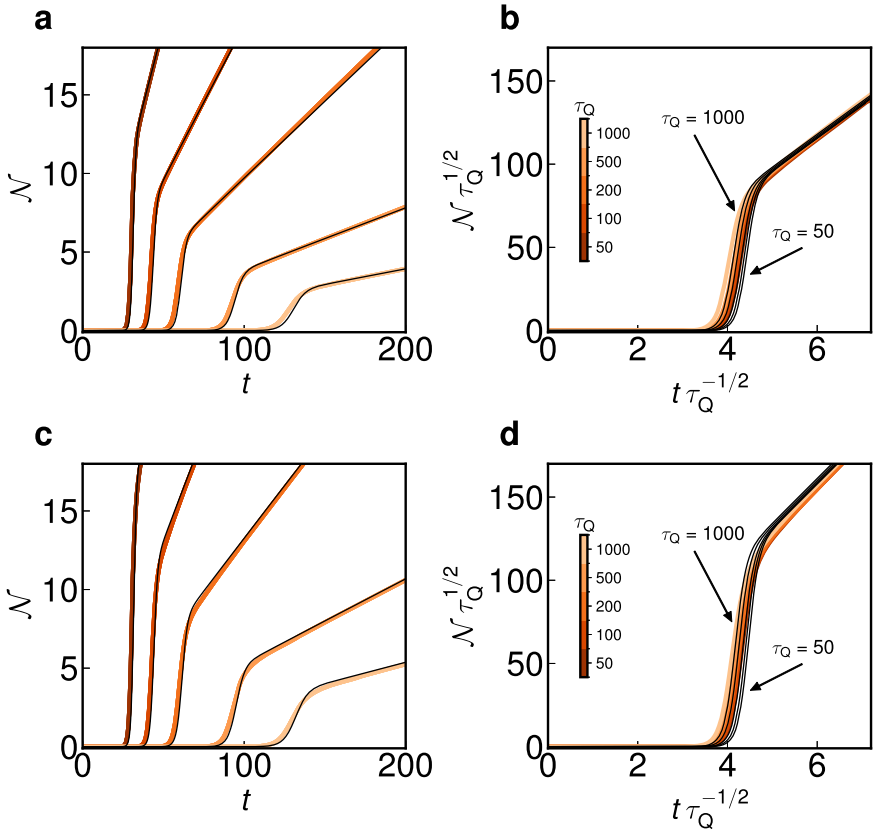


Fig. 2 | Testing the analytical prediction of the condensate norm. a Time evolution of the condensate norm during growth into the immiscible phase for quench times τ_Q = 50, 100, 200, 500, and 1000. Thin black curves show the analytical solution of the condensate norm evolution $\mathcal{N}(t)$ as a function of time t in Eq. 4, in excellent agreement with the numerical results (thick colored curves). **b** Rescaled condensate norm $\mathcal{N}\tau_Q^{1/2}$ plotted as a function of the rescaled time $t\tau_Q^{-1/2}$, demonstrating collapse of the growth curves and universal dynamics. **c** Same as (**a**), but for growth into the miscible phase, where the analytical predictions again closely reproduce the numerical evolution. **d** Rescaled condensate norm $\mathcal{N}\tau_Q^{1/2}$ versus $t\tau_Q^{-1/2}$ for the miscible phase, revealing the same universal growth behavior across different quench times τ_Q.

Here, the total density is $n_T = n_1 + n_2$ and the population imbalance is $n_M = n_1 - n_2$, with $n_1 = |\psi_1|^2$ and $n_2 = |\psi_2|^2$. During the growth stage, population imbalance remains negligible, allowing us to set $n_M = 0$. The evolution equation then reduces to

$$\dot{n}_T - 2\gamma\mu(t)n_T = -\gamma(g + g_{12})n_T^2, \tag{3}$$

which admits an exact solution for the linear quench protocol $\mu(t) = \mu_i + (t/\tau_Q)(\mu_f - \mu_i)$ where μ_i is the initial chemical potential before the quench. The resulting analytical expression for the condensate norm reads

$$\mathcal{N}(t) = n_T(t) = \frac{\mathcal{N}(0)e^{F(t)}}{1 + \mathcal{N}(0)KM(t)}, \tag{4}$$

where $\mathcal{N}(0)$ is the initial number density scaled by the simulation box area at $t = 0$ and $\mathrm{erfi}(x) = 2\int_0^x e^{x'^2}dx'/\sqrt{\pi}$. Here, K, $F(t)$, and $M(t)$ are defined as :

$$K = \gamma(g + g_{12}),$$
$$F(t) = 2\gamma\mu_i t + \frac{\gamma(\mu_f - \mu_i)}{\tau_Q}t^2,$$

and

$$M(t) = \frac{\sqrt{\pi}}{2}\sqrt{\frac{\tau_Q}{\gamma(\mu_f - \mu_i)}}e^{-\frac{\gamma\tau_Q\mu_i^2}{(\mu_f - \mu_i)}}\mathrm{erfi}\left(\sqrt{\frac{\gamma(\mu_f - \mu_i)}{\tau_Q}}t + \sqrt{\frac{\gamma\tau_Q}{(\mu_f - \mu_i)}}\mu_i\right),$$

respectively. The analytical prediction in Eq. 4 quantitatively reproduces the numerical evolution of the condensate norm during growth into the immiscible phase, as shown in Fig. 2a by the thin black curves for quench times τ_Q = 50, 100, 200, 500, and 1000, demonstrating that the early-time condensate growth is well captured by the reduced description. Further, we consider the KZ scaling of the condensate norm. For a periodic system, neglecting thermal noise term, n_T at the equilibration time is proportional to the chemical potential at that time as the system adiabatically follows the change of the chemical potential according to the KZM, giving $n_T(t_{eq}) \propto \tau_Q^{-1/(1+z\nu)}$ and thus $n_T(t) \sim \tau_Q^{-1/(1+z\nu)}f(t/t_{eq}) = \tau_Q^{-1/(1+z\nu)}f(t\tau_Q^{-z\nu/(1+z\nu)})$ for $t \geq t_{eq}$ where $f(x)$ is some arbitrary function depending on x. This is consistent with the results in ref. 53 as $z\nu = 1$ in our case, leading to $\mathcal{N}(t) \sim \tau_Q^{-1/2}f(t\tau_Q^{-1/2})$ and revealing a similar growth dynamics for different τ_Q shown in Fig. 2b. We further analyze the norm evolution analytically in the miscible regime, as shown in Fig. 2c, where the analytical solution again captures the numerical growth of the condensate. In Fig. 2d, we present the appropriately scaled condensate norm, analogous to the immiscible case, and observe a comparable collapse of the curves for different quench times, indicating the same universal growth dynamics.

Phase separated regime and self similar dynamics

Domain formation is a characteristic feature of the immiscible phase, where the two condensate components spontaneously separate in space following the quench, as shown in Fig. 3a–c.

The system initially develops multiple small domains due to phase separation driven by interspecies repulsion, seeded by nonequilibrium fluctuations. The number of domains N_D, measured at $t = t_{eq}$, follows a power-law scaling with the quench time τ_Q, given by $N_D \propto \tau_Q^{-2\nu/(1+z\nu)}$[40]. The determination of N_D from an ensemble of numerical stochastic realizations is discussed in the Supplementary Note 2. This inverse scaling indicates that slower quenches allow more time near t_{eq}, promoting larger correlated regions and fewer domains. The extracted exponent $2\nu/(1 + z\nu)$ yields values of 0.48 ± 0.017 and 0.49 ± 0.024 for the two species, as shown in Fig. 3d, averaged over 100 noise realizations. These irregular domains evolve over time $t > t_{eq}$, with the total number N_D decreasing via domain coarsening —a process that merges adjacent regions to reduce interfacial energy by shortening domain walls. Each domain wall separates high- and low-density regions, with the total length L following the KZM scaling $L \propto \tau_Q^{-(D-d)\nu/(1+z\nu)}$ for $d = 1$ and $D = 2$[48]. At $t = t_{eq}$, the fitted exponent $(D - d)\nu/$

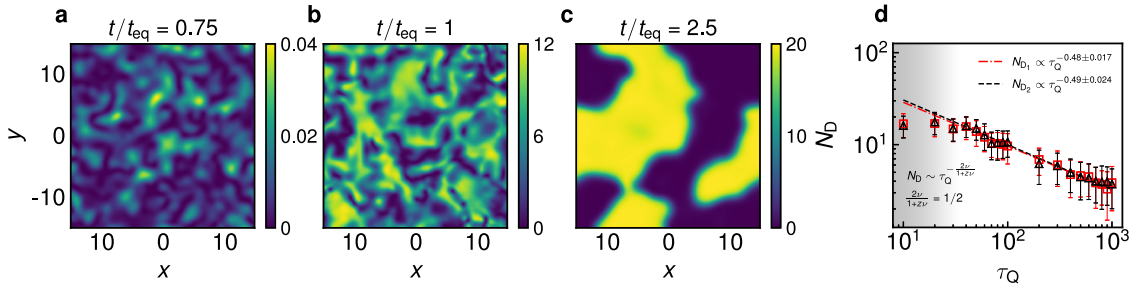
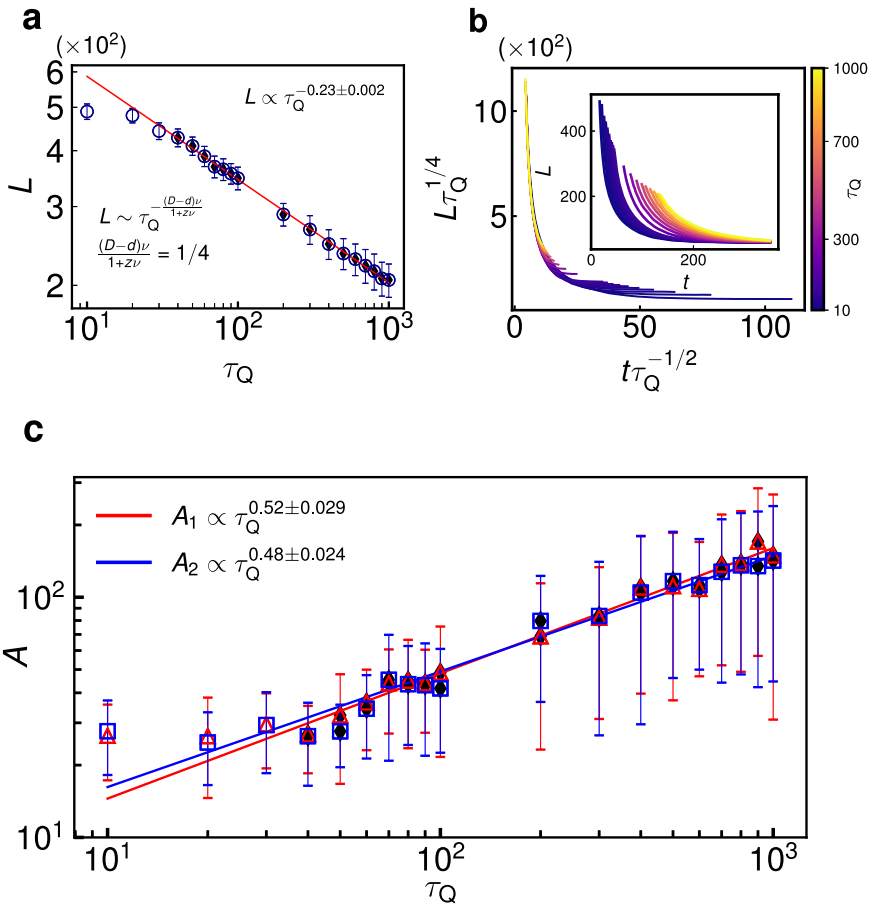


Fig. 3 | Condensate density evolution of the component 1 of the binary Bose–Bose mixture in the immiscible phase. a–c Show domain formation and evolution as a function of time t scaled by the equilibration time t_{eq} at the quench time $\tau_Q = 50$, corresponding to red markers in Fig. 1a. Color bars represent the norm of the condensate order parameter. **d** Shows the domain number N_D as a function of τ_Q on a log scale, revealing the Kibble–Zurek mechanism (KZM) scaling: $N_{D_1} \propto \tau_Q^{-0.48\pm0.017}$, $N_{D_2} \propto \tau_Q^{-0.49\pm0.024}$. Error bars show standard deviations across 100 noise realizations. Gray shaded area in (**d**) denotes deviation from universal KZM behavior, indicating a smooth crossover between fast and slow quenches.

Fig. 4 | Universality of the domain wall in the immiscible phase. a Average domain wall length L for $|\psi_1|^2$ at the equilibration time t_{eq} as a function of the quench time τ_Q (log scale), averaged over 100 runs, showing $L \propto \tau_Q^{-0.23\pm0.002}$. **b** Evolution of L as a function of time t, rescaled by $\tau_Q^{1/4}$, for various τ_Q; inset shows unscaled L as a function of t from t_{eq}. **c** Mean domain area A as a function of τ_Q, showing Kibble–Zurek scaling: $A_1 \propto \tau_Q^{0.52\pm0.029}$, $A_2 \propto \tau_Q^{0.48\pm0.024}$. Error bars show standard deviations over 100 noise realizations.



$(1 + z\nu)$ equals 0.23 ± 0.002 and agree well with the theoretical prediction, as shown in Fig. 4a.

Regardless of τ_Q, the system finally relaxes towards a macroscopic phase-separated state with L saturating to a value dependent on the system size. For $t \geqslant t_{eq}$, the domain wall length L scales as $L \sim \tau_Q^{-\nu/(1+z\nu)} f(t\tau_Q^{-z\nu/(1+z\nu)}) \sim \tau_Q^{-1/4} f(t\tau_Q^{-1/2})$, mathematically consistent form with the results in ref. 48 and demonstrating universal collapse before the system reaches the equilibrium steady state. This is shown in Fig. 4b.

The mean domain area of the respective components at $t = t_{eq}$ also scales with the quench time τ_Q as $A_1 \propto \tau_Q^{0.52\pm0.029}$ and $A_2 \propto \tau_Q^{0.48\pm0.024}$ shown in Fig. 4c. The domain characterization, including labeling, mean area, and wall detection, is detailed in the Supplementary Note 2.

Miscible phase and vortex formation

In the miscible phase ($g_{12} < g$), vortices spontaneously emerge as a hallmark of the KZM, which governs nonequilibrium dynamics after a continuous phase transition. During post-quench evolution, the condensate fragments into protodomains with uncorrelated phases. As domains merge, relative phase differences generate equal number of quantized vortices and antivortices with circulation quantized by the Feynman–Onsager rule[54–56].

For $t \gg t_{eq}$ with any τ_Q considered here, following vortex-antivortex annihilation, the system relaxes into a low-energy miscible state with complete spatial overlap of the two components.

We determine the vortex number at the equilibration time t_{eq}, the moment when well-formed vortex cores first become clearly identifiable in the density profile [Fig. 5a–c], marking the maximum in the number of

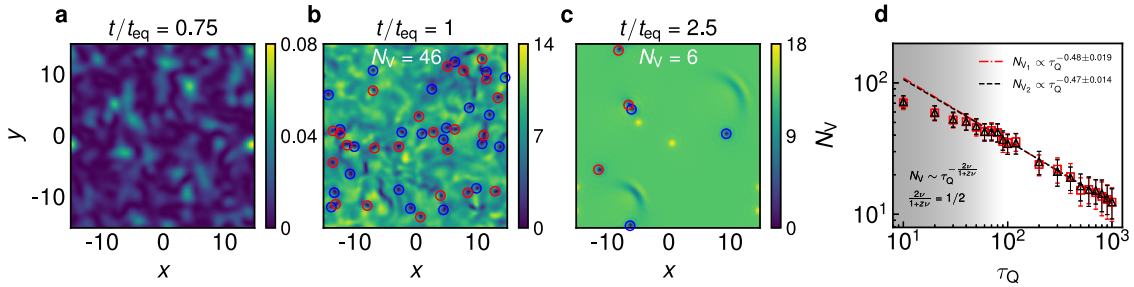


Fig. 5 | Condensate density evolution of the component 1 of the binary Bose–Bose mixture in the miscible phase. a–c Show vortex formation as a function of time t scaled by the equilibration time t_{eq} at the quench time $\tau_Q = 50$, corresponding to red markers in Fig. 1c. **a–c** Highlight the vortex core formation, with blue/red dots indicating positive/negative winding numbers. Color bars represent the norm of the condensate order parameter. **d** Shows the scaling of the vortex number N_V: $N_{V_1} \propto \tau_Q^{-0.48\pm0.019}$, $N_{V_2} \propto \tau_Q^{-0.47\pm0.014}$, averaged over 100 noise realizations. Error bars show standard deviations across these realizations. Gray shaded area in (**d**) denotes deviation from universal Kibble–Zurek mechanism behavior, indicating a smooth crossover between fast and slow quenches.

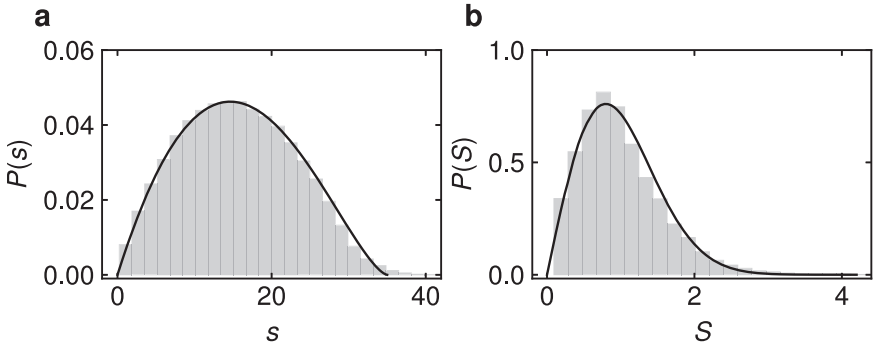


Fig. 6 | Testing Poisson point process predictions on vortex spatial statistics in the miscible phase. **a** Vortex distance distribution, regardless of the charge, for the component 1 of the binary Bose–Bose mixture at the scaled time $t/t_{eq} = 0.930$ with the quench time $\tau_Q = 50$, where s is the distance and t_{eq} is the equilibration time. The solid line corresponds to the disk line-picking formula with disk radius $R = 17.5$ and 25 bins. **b** The first nearest-neighbor spacing distribution of vortices for the same component and quench time, as a function of the normalized spacing $S = s/\bar{s}$ with $\bar{s}$ being the mean nearest-neighbor distance, fitted with Eq. 6 with $k = 1$ (solid line). Histograms are constructed with data from 400 noise realizations.

visible vortex cores before subsequently decreasing as a result of annihilation. Notably, in the miscible phase, the vortex or antivortex cores in one component are filled by atoms of the other, forming coreless vortices. The yellow dots in Fig. 5c signify this and confirm the presence of coreless vortices in ψ_2[57–59]. All of these features have been revealed by our simulations. The quench time dependence of the vortex number N_V is shown in Fig. 5d, revealing the KZM scaling for point defects ($d = 0$) in 2D: $N_{V_1} \propto \tau_Q^{-0.48\pm0.019}$ and $N_{V_2} \propto \tau_Q^{-0.47\pm0.014}$ for the two components.

Universal spatial statistics

While KZM predicts universal scaling of the average defect density and domain-wall length with the quench time, it does not specify how defects are arranged in space or whether their spatial correlations exhibit additional universal features. In particular, KZM does not address whether defect positions are correlated, clustered, or randomly distributed at the time of formation. Motivated by recent studies highlighting the role of spatial statistics as an independent probe of nonequilibrium universality[23,60,61], we therefore analyze the full spatial distributions of vortices in the miscible phase and of mean domain positions in the immiscible phase. By examining distance and nearest-neighbor spacing distributions across many realizations, we test whether defect configurations are consistent with PPP determined solely by the KZ defect density, thereby extending universality from scaling laws to stochastic-geometric properties of defect patterns.

During growth into the miscible phase, vortices and antivortices emerge at random positions within each superfluid component at $t \sim t_{eq}$, with positions varying across noise realizations. To reveal emergent spatial correlations, we analyze vortex-vortex and mean domain positions (geometric centroids, see the Supplementary Note 3) statistics using a homogeneous PPP model, where defect density is governed by the KZM[23,60,62].

Accordingly, the vortex distance distribution $P(s)$ is expected to follow a uniform distribution over a disk of radius R, described by the disk line-picking formula[23,63]:

$$P(s) = \frac{4s}{\pi R^2}\left[\arccos\left(\frac{s}{2R}\right) - \frac{s}{2R}\sqrt{1-\frac{s^2}{4R^2}}\right]. \quad (5)$$

By aggregating data across all realizations, we smooth out realization-specific randomness and reveal the underlying universal geometric structure of defect positions, which matches well with PPP predictions (Fig. 6a).

For further characterization, we compute the first nearest-neighbor spacing statistics for vortex positions and mean domain positions in each component[23,60]. For each vortex, the probability of finding its nearest neighbor in a shell between s and $s + ds$ is evaluated, ensuring that other vortices lie beyond radius s. This is repeated across all vortices and realizations. The kth—order spacing distribution is given by refs. 64, 65,

$$P_k(S) = \frac{2}{(k-1)!}\, r^{2k}\, S^{2k-1}\, e^{-r^2S^2}, \quad (6)$$

where $r = \Gamma(k+\frac{1}{2})/\Gamma(k)$. The spacings are normalized by the mean nearest-neighbor distance $\bar{s}$, and the resulting normalized spacings $S = s/\bar{s}$ give the final distribution. For vortices, the spacing distribution follows the Wigner–Dyson form $P(S) = \frac{\pi}{2} S \exp\left(-\frac{\pi}{4}S^2\right)$, as shown in Fig. 6b with $k = 1$. A similar analysis in the immiscible phase shows that the mean domain positions also follow Poisson statistics (Fig. 7a), revealing a comparable geometric structure at the onset of phase separation. Further, the first nearest-neighbor statistics of the mean domain positions yields a spacing distribution, which is in good agreement with the Eq. 6 with $k = 2$, shown in the Fig. 7b. This occurs because the size of domains are finite and also a domain of one component is often separated from its nearest neighbor by a domain of the other component, as seen in the inset of Fig. 7b. These results reveal strong spatial correlations and universal spacing statistics in both

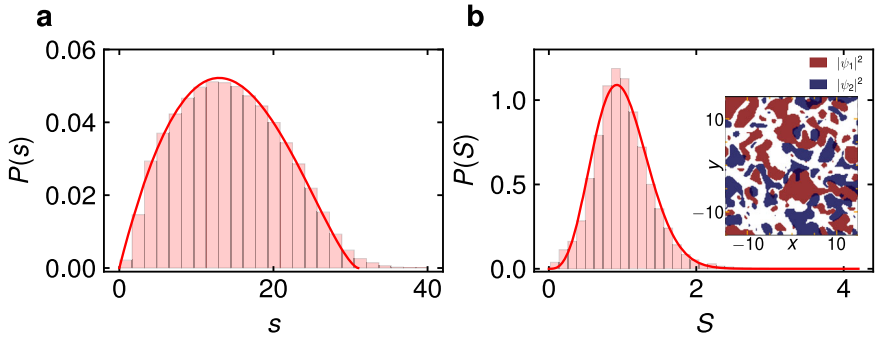


Fig. 7 | Testing Poisson point process predictions on domain spatial statistics in the immiscible phase. a Domain distance distribution for the component 1 of the binary Bose–Bose mixture at the scaled time $t/t_{eq} = 0.930$ with the quench time $\tau_Q = 50$, where s is the distance and t_{eq} is the equilibration time. The solid line corresponds to the disk line-picking formula with disk radius $R = 15.5$ and 25 bins. **b** Further, the first nearest-neighbor spacing distribution for mean domain positions, as a function of the normalized spacing $S = s/\bar{s}$ with $\bar{s}$ being the mean nearest-neighbor distance, follows Eq. 6 with $k = 2$ (solid line). The distributions are computed at $t/t_{eq} = 0.930$ for $\tau_Q = 50$, using 25-bin histograms constructed from 400 noise realizations. (Inset) Density profiles $|\psi_j|^2$ of both components ($j = 1, 2$) at $t/t_{eq} = 0.930$, plotted together using a threshold of 50% of the maximum density (see the Supplementary Note 2), from a single noise realization.

vortex and domain configurations. Similar features are displayed by the $j = 2$ component, as shown in the Supplementary Note 3.

Note that two different components in the binary BEC (ψ_1 and ψ_2) are coupled via the inter-species interaction coefficient g_{12}, affecting each other. Therefore, it is not trivial that the homogeneous PPP can be applied beyond the single-component system, because positions of defects in one component could be affected by positions of defects in other components (as in Eto et al.[66]), possibly breaking "randomly and independently distributed" assumption of the homogeneous PPP for positions of defects in each component. Yet, our findings show that our KZM-PPP model is valid even for defects in the binary BEC (component 1 and component 2, respectively), at least around the equilibration time t_{eq} from when defects can be visibly detected in the density profile. Indeed, as time goes on, the first nearest neighbor spacing distribution deviates from our KZM-PPP model, as shown in the Supplementary Note 3. Still, our results imply that the initial positions of defects in each component could be considered as "randomly and independently distributed" points, even if there are interactions between different components.

As a final remark, since our KZM-PPP model does not take into account the detailed form of the interaction between defects, it could also be applied to any multi-component system beyond the BEC.

Conclusions

We have shown that symmetry-breaking transitions in a homogeneous binary superfluid, driven by a linear quench, exhibit universal dynamics consistent with the Kibble–Zurek mechanism, which can be extended to account for the fluctuations in the number and spatial distribution of topological defects. Our results can be experimentally tested using atomic mixtures confined in uniform traps, which are ideally suited to probe dynamical scaling laws without causality-induced corrections ubiquitous in inhomogeneous systems[16,33–35,67].

We anticipate that the spatial distribution of topological defects in quantum gas mixtures is of relevance to other scenarios, such as the spontaneous emergence of quantum turbulence after a quench[61,68]. In such a context, the incompressible kinetic energy in each component is affected by the vortex positions in the corresponding component, motivating the extension of the previous[69–71] results to multi-component systems. A complementary approach concerns the study of the circulation statistics within an arbitrary area in each component and explore extensions of Migdal's area rule[61,72].

Methods

We study the dynamics of symmetry-breaking associated with the emergence of nonzero complex order parameters that pertain to the formation of miscible and immiscible (phase-separated) phases in a steady-state 2D homogeneous Bose–Bose mixture. To establish a reliable theoretical framework that captures the effects of fluctuations in the dynamics of continuous symmetry-breaking phase transitions, we resort to the SPGPE[44,45,73–88], given by

$$i\hbar\frac{\partial}{\partial t}\psi_j(\mathbf{x},t) = \widehat{\mathcal{P}}\left\{(1-i\gamma)\left[\left(-\frac{\hbar^2\nabla^2}{2m} + g|\psi_j(\mathbf{x},t)|^2 + g_{12}|\psi_{3-j}|^2 - \mu(t)\right)\psi_j\right] + \eta_j(\mathbf{x},t)\right\}, \tag{7}$$

where $\mathbf{x} \equiv (x, y)$ and ∇^2 are the Cartesian coordinates and Laplacian operator in 2D respectively. With γ being the dissipation parameter, $\psi_j(\mathbf{x}, t)$ represents the classical (**C**) field for each component (species) $j \in 1, 2$, describing the macroscopically occupied low-energy modes subject to random thermal fluctuations represented by the stochastic Gaussian noise term η_j. The projector $\widehat{\mathcal{P}}$ constrains the **C** field to the coherent region at each time step (see the Supplementary Methods).

The intra- and inter-species interaction strengths are denoted by g and g_{12}, respectively. Starting from a disordered symmetric phase with $\psi_j = 0$, the system experiences symmetry breaking and transitions to an ordered miscible or immiscible phase depending on the relative values of g and g_{12}, as the chemical potential μ is tuned from below to above the critical point. We implement a linear ramping of the chemical potential $\mu(t) = \mu_i + (t/\tau_Q)(\mu_f - \mu_i)$, with τ_Q being the time of the linear quench. At time $t = 0$, the initial chemical potential is $\mu_i = 0.1$, and is linearly ramped up to the final chemical potential $\mu_f = 20$ at different quench rates $1/\tau_Q$. We perform numerical simulations to investigate the dynamics of the transition to the miscible ($g_{12}/g = 0.5$) and immiscible ($g_{12}/g = 1.05$) phases with $g = 1$ in a box of size $\mathcal{A} = 30 \times 30$. Defining E_{sc} as the energy scale, the length, temperature, and time are measured in units of $\sqrt{\hbar^2/mE_{sc}}$, E_{sc}/k_B, and $\hbar/E_{sc}$, respectively, where $\hbar$ is the reduced Planck's constant and k_B is the Boltzmann constant. For convenience, we set $E_{sc} = \mu_{f,p}/20$ where $\mu_{f,p}$ is the final chemical potential in physical units (around $k_B \times 0.7$ nK if one uses the same parameters in the quasi-two-dimensional BEC experiment[52]). Additionally, since γ does not affect the exponents on the KZ scaling laws[89,90], we set $\gamma = 0.05$.

Data availability

The data that support the findings of this study are available under a "Creative Commons Attribution 4.0 International License" on Zenodo under https://doi.org/10.5281/zenodo.17608491. Representative dynamical evolutions are provided as "Supplementary Movies 1 and 2", illustrating the evolution into the miscible and immiscible regimes, respectively, along with vortex nucleation and domain formation.

Code availability

Codes are available from the corresponding author upon request.

Received: 18 November 2025; Accepted: 21 April 2026;
Published online: 09 May 2026

References

1. Kibble, T. W. B. Topology of cosmic domains and strings. *J. Phys. A Math. Gen.* **9**, 1387 (1976).
2. Kibble, T. Some implications of a cosmological phase transition. *Phys. Rep.* **67**, 183 (1980).
3. Morikawa, M. Cosmological inflation as a quantum phase transition. *Prog. Theor. Phys.* **93**, 685 (1995).
4. Bäuerle, C., Bunkov, Y. M., Fisher, S. N., Godfrin, H. & Pickett, G. R. Laboratory simulation of cosmic string formation in the early universe using superfluid ^{3}He. *Nature* **382**, 332 (1996).
5. Ruutu, V. M. H. et al. Vortex formation in neutron-irradiated superfluid ^{3}He as an analogue of cosmological defect formation. *Nature* **382**, 334 (1996).
6. Monaco, R., Mygind, J., Rivers, R. J. & Koshelets, V. P. Spontaneous fluxoid formation in superconducting loops. *Phys. Rev. B.* **80**, 180501 (2009).
7. Zurek, W. H. Cosmological experiments in superfluid helium? *Nature* **317**, 505 (1985).
8. Ueda, M. *Fundamentals and New Frontiers of Bose-Einstein Condensation* (World Scientific, 2010).
9. Stamper-Kurn, D. M. & Ueda, M. Spinor Bose gases: symmetries, magnetism, and quantum dynamics. *Rev. Mod. Phys.* **85**, 1191–1244 (2013).
10. del Campo, A. & Zurek, W. H. Universality of phase transition dynamics: topological defects from symmetry breaking. *Int. J. Mod. Phys. A.* **29**, 1430018 (2014).
11. Keesling, A. et al. Quantum Kibble-Zurek mechanism and critical dynamics on a programmable Rydberg simulator. *Nature* **568**, 207 (2019).
12. Chepiga, N. & Mila, F. Kibble-Zurek exponent and chiral transition of the period-4 phase of Rydberg chains. *Nat. Commun.* **12**, 145 (2021).
13. Ebadi, S. et al. Quantum phases of matter on a 256-atom programmable quantum simulator. *Nature* **595**, 227 (2021).
14. Zurek, W. Cosmological experiments in condensed matter systems. *Phys. Rep.* **276**, 177 (1996).
15. Weiler, C. N. et al. Spontaneous vortices in the formation of Bose-Einstein condensates. *Nature* **455**, 948 (2008).
16. Zurek, W. H. Causality in condensates: gray solitons as relics of BEC formation. *Phys. Rev. Lett.* **102**, 105702 (2009).
17. Lamporesi, G., Donadello, S., Serafini, S., Dalfovo, F. & Ferrari, G. Spontaneous creation of Kibble-Zurek solitons in a Bose-Einstein condensate. *Nat. Phys.* **9**, 656 (2013).
18. Navon, N., Gaunt, A. L., Smith, R. P. & Hadzibabic, Z. Critical dynamics of spontaneous symmetry breaking in a homogeneous Bose gas. *Science* **347**, 167 (2015).
19. Clark, L. W., Feng, L. & Chin, C. Universal space-time scaling symmetry in the dynamics of bosons across a quantum phase transition. *Science* **354**, 606 (2016).
20. Feng, L., Clark, L. W., Gaj, A. & Chin, C. Coherent inflationary dynamics for Bose-Einstein condensates crossing a quantum critical point. *Nat. Phys.* **14**, 269 (2018).
21. Ko, B., Park, J. W. & Shin, Y. Kibble-Zurek universality in a strongly interacting Fermi superfluid. *Nat. Phys.* **15**, 1227–1231 (2019).
22. Goo, J., Lim, Y. & Shin, Y. Defect saturation in a rapidly quenched Bose gas. *Phys. Rev. Lett.* **127**, 115701 (2021).
23. Thudiyangal, M. & del Campo, A. Universal vortex statistics and stochastic geometry of Bose-Einstein condensation. *Phys. Rev. Res.* **6**, 033152 (2024).
24. Anquez, M. et al. Quantum Kibble-Zurek mechanism in a spin-1 Bose-Einstein condensate. *Phys. Rev. Lett.* **116**, 155301 (2016).
25. Prüfer, M. et al. Observation of universal dynamics in a spinor Bose gas far from equilibrium. *Nature* **563**, 217 (2018).
26. Baroni, C., Lamporesi, G. & Zaccanti, M. Quantum mixtures of ultracold gases of neutral atoms. *Nat. Rev. Phys.* **6**, 736–752 (2024).
27. Ho, T.-L. & Shenoy, V. B. Binary mixtures of Bose condensates of alkali atoms. *Phys. Rev. Lett.* **77**, 3276 (1996).
28. Hofmann, J., Natu, S. S. & Das Sarma, S. Coarsening dynamics of binary Bose condensates. *Phys. Rev. Lett.* **113**, 095702 (2014).
29. Trippenbach, M., Góral, K., Rzążewski, K., Malomed, B. & Band, Y. B. Structure of binary Bose-Einstein condensates. *J. Phys. B.* **33**, 4017 (2000).
30. Donadello, S. et al. Creation and counting of defects in a temperature-quenched Bose-Einstein condensate. *Phys. Rev. A.* **94**, 023628 (2016).
31. Scherer, D. R., Weiler, C. N., Neely, T. W. & Anderson, B. P. Vortex formation by merging of multiple trapped Bose-Einstein condensates. *Phys. Rev. Lett.* **98**, 110402 (2007).
32. del Campo, A., Retzker, A. & Plenio, M. B. The inhomogeneous Kibble-Zurek mechanism: vortex nucleation during Bose-Einstein condensation. *New J. Phys.* **13**, 083022 (2011).
33. del Campo, A., Kibble, T. W. B. & Zurek, W. H. Causality and non-equilibrium second-order phase transitions in inhomogeneous systems. *J. Phys. Condens. Matter* **25**, 404210 (2013).
34. Ulm, S. et al. Observation of the Kibble–Zurek scaling law for defect formation in ion crystals. *Nat. Commun.* **4**, 2290 (2013).
35. Pyka, K. et al. Topological defect formation and spontaneous symmetry breaking in ion Coulomb crystals. *Nat. Commun.* **4**, 2291 (2013).
36. Cui, J.-M. et al. Experimentally testing quantum critical dynamics beyond the Kibble-Zurek mechanism. *Commun. Phys.* **3**, 44 (2020).
37. Reichhardt, C. J. O., del Campo, A. & Reichhardt, C. Kibble-Zurek mechanism for nonequilibrium phase transitions in driven systems with quenched disorder. *Commun. Phys.* **5**, 173 (2022).
38. Maegochi, S., Ienaga, K. & Okuma, S. Kibble-Zurek mechanism for dynamical ordering in a driven vortex system. *Phys. Rev. Lett.* **129**, 227001 (2022).
39. Monaco, R., Mygind, J., Aaroe, M., Rivers, R. J. & Koshelets, V. P. Zurek-Kibble mechanism for the spontaneous vortex formation in Nb-Al/Al_{ox}/Nb Josephson tunnel junctions: new theory and experiment. *Phys. Rev. Lett.* **96**, 180604 (2006).
40. Wu, S., Ke, Y., Huang, J. & Lee, C. Kibble-zurek scalings of continuous magnetic phase transitions in spin-1 spin-orbit-coupled Bose-Einstein condensates. *Phys. Rev. A.* **95**, 063606 (2017).
41. Sabbatini, J., Zurek, W. H. & Davis, M. J. Phase separation and pattern formation in a binary Bose-Einstein condensate. *Phys. Rev. Lett.* **107**, 230402 (2011).
42. Sabbatini, J., Zurek, W. H. & Davis, M. J. Causality and defect formation in the dynamics of an engineered quantum phase transition in a coupled binary Bose-Einstein condensate. *New J. Phys.* **14**, 095030 (2012).
43. Swislocki, T., Witkowska, E., Dziarmaga, J. & Matuszewski, M. Double universality of a quantum phase transition in spinor condensates: modification of the Kibble-Żurek mechanism by a conservation law. *Phys. Rev. Lett.* **110**, 045303 (2013).
44. Ota, M. et al. Collisionless sound in a uniform two-dimensional Bose gas. *Phys. Rev. Lett.* **121**, 145302 (2018).
45. Proukakis, N. P. & Jackson, B. Finite-temperature models of Bose-Einstein condensation. *J. Phys. B.* **41**, 203002 (2008).
46. Chesler, P. M., García-García, A. M. & Liu, H. Defect formation beyond Kibble-Zurek mechanism and holography. *Phys. Rev. X* **5**, 021015 (2015).

47. del Campo, A. et al. Universal statistics of vortices in a newborn holographic superconductor: beyond the Kibble-Zurek mechanism. *J. High Energy Phys.* **2021**, 061 (2021).
48. Ma, T.-C., Shi, H.-Q., Zhang, H.-Q. & del Campo, A. Universal critical holography and domain wall formation. *Phys. Rev. Res.* **7**, 013096 (2025).
49. Campostrini, M., Hasenbusch, M., Pelissetto, A., Rossi, P. & Vicari, E. Critical behavior of the three-dimensional XY universality class. *Phys. Rev. B.* **63**, 214503 (2001).
50. Gómez-Ruiz, F. J., Mayo, J. J. & del Campo, A. Full counting statistics of topological defects after crossing a phase transition. *Phys. Rev. Lett.* **124**, 240602 (2020).
51. Giorgetti, L., Carusotto, I. & Castin, Y. Semiclassical field method for the equilibrium Bose gas and application to thermal vortices in two dimensions. *Phys. Rev. A.* **76**, 013613 (2007).
52. Chomaz, L. et al. Emergence of coherence via transverse condensation in a uniform quasi-two-dimensional Bose gas. *Nat. Commun.* **6**, 6162 (2015).
53. Suzuki, F. & Zurek, W. H. Deconstructing dynamics of symmetry breaking. *Proc. Natl. Acad. Sci. USA* **122**, e2523903122 (2025).
54. Onsager, L. Statistical hydrodynamics. *Il Nuovo Cimento* **6**, 279 (1949).
55. Feynman, R. P. Application of quantum mechanics to liquid helium. In (ed Gorter, C. J.) *Progress in Low Temperature Physics*, Vol. 1, 17 (Elsevier, 1955).
56. Donnelly, R. J. *Quantized Vortices in Helium II* (Cambridge University Press, 1991).
57. Wheeler, M. T., Salman, H. & Borgh, M. O. Relaxation dynamics of half-quantum vortices in a two-dimensional two-component Bose-Einstein condensate(a). *EPL* **135**, 30004 (2021).
58. Ji, A.-C., Liu, W. M., Song, J. L. & Zhou, F. Dynamical creation of fractionalized vortices and vortex lattices. *Phys. Rev. Lett.* **101**, 010402 (2008).
59. Gautam, S., Muruganandam, P. & Angom, D. Coreless vortex dipoles and trapped droplets in phase-separated binary condensates. *J. Phys. B.* **45**, 055303 (2012).
60. del Campo, A., Gómez-Ruiz, F. J. & Zhang, H.-Q. Locality of spontaneous symmetry breaking and universal spacing distribution of topological defects formed across a phase transition. *Phys. Rev. B.* **106**, L140101 (2022).
61. Massaro, M., Shinn, S.-H., Thudiyangal, M. & del Campo, A. Circulation statistics and Migdal area rule beyond the Kibble-Zurek mechanism in a newborn Bose-Einstein condensate. Preprint at https://doi.org/10.48550/arXiv.2508.11047 (2025).
62. Massaro, M. & del Campo, A. Spatial form factor for point patterns: Poisson point process, Coulomb gas, and vortex statistics. *Phys. Rev. Res.* **7**, 023107 (2025).
63. Mathai, A. M. *An Introduction to Geometrical Probability: Distributional Aspects with Applications*, Vol. 1 (CRC Press, 1999).
64. Haake, F. *Quantum Signatures of Chaos,* 2nd edn (Springer, 2001).
65. Sakhr, J. & Nieminen, J. M. Wigner surmises and the two-dimensional homogeneous Poisson point process. *Phys. Rev. E.* **73**, 047202 (2006).
66. Eto, M., Kasamatsu, K., Nitta, M., Takeuchi, H. & Tsubota, M. Interaction of half-quantized vortices in two-component Bose-Einstein condensates. *Phys. Rev. A.* **83**, 063603 (2011).
67. Kim, M. et al. Suppression of spontaneous defect formation in inhomogeneous Bose gases. *Phys. Rev. A.* **106**, L061301 (2022).
68. Shinn, S.-H., Massaro, M., Thudiyangal, M. & del Campo, A. Spontaneous quantum turbulence in a newborn Bose-Einstein condensate via the Kibble-Zurek mechanism. Preprint at https://doi.org/10.48550/arXiv.2506.21670 (2025).
69. Novikov, E. A. Dynamics and statistics of a system of vortices. *Sov. Phys. JETP* **68**, 1868 (1975).
70. Chavanis, P.-H. & Sire, C. The spatial correlations in the velocities arising from a random distribution of point vortices. *Phys. Fluids* **13**, 1904–1923 (2001).
71. Bradley, A. S. & Anderson, B. P. Energy spectra of vortex distributions in two-dimensional quantum turbulence. *Phys. Rev. X* **2**, 041001 (2012).
72. Migdal, A. Statistical equilibrium of circulating fluids. *Phys. Rep.* **1011**, 1–117 (2023).
73. Berloff, N. G., Brachet, M. & Proukakis, N. P. Modeling quantum fluid dynamics at nonzero temperatures. *Proc. Natl. Acad. Sci. USA* **111**, 4675 (2014).
74. Blakie, P., Bradley, A., Davis, M., Ballagh, R. & Gardiner, C. Dynamics and statistical mechanics of ultra-cold Bose gases using c-field techniques. *Adv. Phys.* **57**, 363 (2008).
75. Bradley, A. S., Gardiner, C. W. & Davis, M. J. Bose-Einstein condensation from a rotating thermal cloud: vortex nucleation and lattice formation. *Phys. Rev. A.* **77**, 033616 (2008).
76. Brewczyk, M., Gajda, M. & Rzażewski, K. Classical fields approximation for bosons at nonzero temperatures. *J. Phys. B.* **40**, R1 (2007).
77. Cockburn, S. P. & Proukakis, N. P. The stochastic Gross-Pitaevskii equation and some applications. *Laser Phys.* **19**, 558 (2009).
78. Bradley, A. S. & Blakie, P. B. Stochastic projected Gross-Pitaevskii equation for spinor and multicomponent condensates. *Phys. Rev. A.* **90**, 023631 (2014).
79. Gallucci, D. & Proukakis, N. P. Engineering dark solitary waves in ring-trap Bose-Einstein condensates. *New J. Phys.* **18**, 025004 (2016).
80. Kobayashi, M. & Cugliandolo, L. F. Thermal quenches in the stochastic Gross-Pitaevskii equation: morphology of the vortex network. *EPL* **115**, 20007 (2016).
81. Proukakis, N. P., Schmiedmayer, J. & Stoof, H. T. C. Quasicondensate growth on an atom chip. *Phys. Rev. A.* **73**, 053603 (2006).
82. Proukakis, N., Gardiner, S., Davis, M. & Szymańska, M. *Quantum Gases: Finite Temperature and Non-Equilibrium Dynamics* (Imperial College Press, 2011).
83. Rooney, S. J., Neely, T. W., Anderson, B. P. & Bradley, A. S. Persistent-current formation in a high-temperature Bose-Einstein condensate: an experimental test for classical-field theory. *Phys. Rev. A.* **88**, 063620 (2013).
84. Stoof, H. T. C. & Bijlsma, M. J. Dynamics of fluctuating Bose-Einstein condensates. *J. Low. Temp. Phys.* **124**, 431 (2001).
85. Su, S.-W. et al. Spontaneous crystallization of skyrmions and fractional vortices in fast-rotating and rapidly quenched spin-1 Bose-Einstein condensates. *Phys. Rev. A.* **84**, 023601 (2011).
86. Rooney, S. J. *Implementation and Applications of the Stochastic Projected Gross-Pitaevskii Equation*. PhD thesis, Univ. of Otago (2015).
87. Roy, A., Ota, M., Recati, A. & Dalfovo, F. Finite-temperature spin dynamics of a two-dimensional Bose-Bose atomic mixture. *Phys. Rev. Res.* **3**, 013161 (2021).
88. Underwood, A. P. C. & Blakie, P. B. Stochastic Gross-Pitaevskii theory for a spin-1 Bose gas: application to superfluidity in two dimensions. *Phys. Rev. A.* **112**, 023315 (2025).
89. Kasamatsu, K., Tsubota, M. & Ueda, M. Nonlinear dynamics of vortex lattice formation in a rotating Bose-Einstein condensate. *Phys. Rev. A* **67**, 033610 (2003).
90. Damski, B. & Zurek, W. H. Soliton creation during a Bose-Einstein condensation. *Phys. Rev. Lett.* **104**, 160404 (2010).

Acknowledgements

We thank Sunil Kumar V. and Sivasankar P.M. for several insightful discussions. Stimulating discussions with Aridaman Singh Chauhan and Subhajit Paul during the early stages of the work are further acknowledged. A.R., S.P. acknowledge the support of the Science and Engineering

Research Board (SERB), Department of Science and Technology, Government of India, under the project SRG/2022/000057 and IIT Mandi seed-grant funds under the project IITM/SG/AR/87; S.S., A.d.C. acknowledge financial support from the Luxembourg National Research Fund under grant no. C22/MS/17132060/BeyondKZM; M.T. acknowledges the support of Anusandhan National Research Foundation (ANRF), Government of India, through the Prime Minister early career grant ANRF/ECRG/2024/003150/PMS, and Christ University for funding the research through the seed grant, sanction No. CU-ORS-SM-24/94. A.R., S.P. acknowledge the National Supercomputing Mission (NSM) for providing computing resources of PARAM Himalaya at IIT Mandi, which is implemented by C-DAC and supported by the Ministry of Electronics and Information Technology (MeitY) and Department of Science and Technology (DST), Government of India.

Author contributions

M.T. conceptualized the problem, and S.P., M.T., and A.R. initiated the project. S.P. performed all numerical simulations. All authors, including A.d.C., S.S., participated in the discussions, data analysis, and writing of the manuscript.

Funding

The authors received no specific funding for this work.

Competing interests

The authors declare no competing interests.

Additional information

Supplementary information The online version contains Supplementary material available at https://doi.org/10.1038/s42005-026-02668-7.

Correspondence and requests for materials should be addressed to Arko Roy.

Peer review information *Communications Physics* thanks the anonymous reviewers for their contribution to the peer review of this work.

Reprints and permissions information is available at http://www.nature.com/reprints

Publisher's note Springer Nature remains neutral with regard to jurisdictional claims in published maps and institutional affiliations.

Open Access This article is licensed under a Creative Commons Attribution-NonCommercial-NoDerivatives 4.0 International License, which permits any non-commercial use, sharing, distribution and reproduction in any medium or format, as long as you give appropriate credit to the original author(s) and the source, provide a link to the Creative Commons licence, and indicate if you modified the licensed material. You do not have permission under this licence to share adapted material derived from this article or parts of it. The images or other third party material in this article are included in the article's Creative Commons licence, unless indicated otherwise in a credit line to the material. If material is not included in the article's Creative Commons licence and your intended use is not permitted by statutory regulation or exceeds the permitted use, you will need to obtain permission directly from the copyright holder. To view a copy of this licence, visit http://creativecommons.org/licenses/by-nc-nd/4.0/.

© The Author(s) 2026